Onset of evaporation-driven gravitational instability in a saline solution

Min Chan Kim[†]

Department of Chemical Engineering, Jeju National University, Jeju 63243, Korea
(*Received 20 July 2020 • Revised 12 August 2020 • Accepted 1 September 2020*)

Abstract–The onset time of buoyancy-driven instability in a saline solution where evaporation proceeds through the solution-air interface is analyzed theoretically and numerically. Based on linear stability theory, new stability equations are derived and numerically solved. Also, nonlinear numerical simulations are conducted using FEM solver, COMSOL Multiphysics.® It is clearly shown that as the evaporation proceeds, the height of solution continuously decreases with time. Moreover, as the evaporation proceeds, concentrated saline solution near the evaporating surface induces gravitational instability. The critical time determined from the linear stability analysis explains the numerical simulation results reasonably. The present theoretical and numerical studies present that evaporation-driven instability is governed by the dimensionless evaporation rate, α, and the initial salt concentration, Ra. The present numerical simulations explain the previous experimental plume dynamics in the evaporation-driven instability systems quite well.

Keywords: Evaporation, Gravitational Instability, Linear Stability Analysis, Numerical Simulation

INTRODUCTION

It has been well-known that in a pure fluid, evaporative convection is driven by temperature gradient induced by removal of heat of evaporation. The onset of evaporative Bénard-Marangoni instability driven by temperature gradient has attracted much research interest [1,2]. However, in a multi-component system, like ethanol-water mixtures, as alcohol evaporates, a concentration gradient develops near the evaporating surface. Therefore, an adverse density gradient is built up, inducing gravitational instability [3]. In addition, in a solution of volatile solvent and involatile solute, the solute gradients generated by a solvent evaporation [4-6] can induce gravitational instability. The evaporation-driven gravitational instability plays an important role in many applications, such as the geotaxis of microorganisms [5] and evaporation of polymer solution [6-8].

Fang et al. [8] and Sobac et al. [9] studied the effect of solvent evaporation rate on the morphology of the polymeric film formed by evaporating a solvent from a polymer solution. According to their experiments, at a lower evaporation rate condition the stable liquid film can be maintained. Therefore, the diffusion-dominant sequential deposition of concentrated precipitates onto the substrate is observed. However, at a high solvent evaporation rate case, instability of the polymer solution can be found. Thus, the movement of the precipitates is dominated by convective fluid flow and downward enrichment area thus evolves. Later, Mossige et al. [6] found that solutions are stable due to the concentration gradients near the polymer-rich interface of dilute long-chain polymer solutions. According to their experiments, in diluted polymer solutions, diffusion does not smear out concentration differences on the time scale of the evaporation-driven instability. As a result, the solution-air interface is remained unperturbed.

Even though much experimental work has been conducted to understand the effect of evaporation rate on the onset and the growth of gravitational instability, less attention has been given to the theoretical prediction of the onset of evaporation-driven instability in involatile solute systems. For a saline water system where water evaporates via water-air interface, Dunstan et al. [5] conducted linear stability analysis by employing a conventional frozen-time model, which is inappropriate for the system having rapldily changing density profile. Dunstan et al. [5] also performed numerical simulation to explain their experimental results. According to their numerical sumulation, downward instability motion exists at the low concentration region of the air-water interface. This is an unexpected result, because the downward motion should be induced by denser region near the interface. Therefore, to understand the evaporation-driven gravitational instabilities, more refined work is needed.

In this study, the effect of evaporation on the onset and the growth of buoyancy-driven instability has been analyzed. For the saline water system, by considering the evaporation of water, we analyzed the onset of gravitational instability using linear stability theory. In addition, to understand the growth of instability, fully nonlinear analysis by using commercial FEM solver, COMSOL Multiphysics, has been conducted. Then, the comparison of the present theoretical and numerical analyses with the previous experimental results follows. The present study provides basic tools to understand the evaporation-driven convection in an industrial process such as pattern formation during the evaporation of the polymer solutions.

BASE SYSTEM AND GOVERNING EQUATIONS

The system considered here is saline solution laid on a flat surface with initial thickness and initial salt concentration d and C_i, respectively. For time t≥0, water evaporates at the free air-solution

---

[†]To whom correspondence should be addressed.
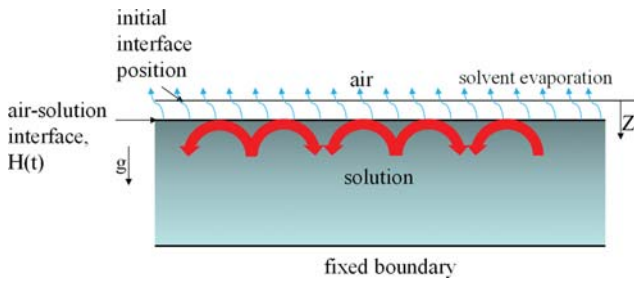E-mail: mckim@cheju.ac.kr

Fig. 1. Schematic diagram of system considered here. As solvent evaporates, the position of air-solution interface moves downward and evaporation-driven instability can be developed.

interface, with salts concentrated near the interface. The interface position moves downward with time, while the total amount of involatile salts in the solution is maintained. A schematic diagram of the basic system of pure diffusion is shown in Fig. 1. The concentration difference driven by water evaporation makes the system unstable and the convective motions will set in at a certain time if the evaporation rate of water is quite enough. By assuming the solution is a Newtonian fluid, the governing equations of flow and concentration fields are expressed as

$$\nabla \cdot \mathbf{U} = 0, \tag{1}$$

$$\rho_r \left\{ \frac{\partial}{\partial t} + \mathbf{U} \cdot \nabla \right\} \mathbf{U} = -\nabla P + \nabla \cdot \{\mu \nabla \mathbf{U} + \mu (\nabla \mathbf{U})^T\} + \rho_r \beta C \mathbf{g}, \tag{2}$$

$$\left\{ \frac{\partial}{\partial t} + \mathbf{U} \cdot \nabla \right\} C = \nabla \cdot (D \nabla C). \tag{3}$$

under the Boussinesq approximation. $\mathbf{U}$, P, ρ_r, $\beta\{=\rho_r^{-1}(\partial\rho/\partial C)\}$, $\mathbf{g}$, μ, C, and D represent the velocity vector, the pressure, the density, the densification coefficient, the gravitational acceleration, the viscosity, the concentration and the diffusivity, respectively. The subscript "r" represents the reference state which is chosen as water in the present study.

Prior to the onset of convective motion, the salt concentration field is governed by

$$\frac{\partial C_0}{\partial t} = D \frac{\partial^2 C_0}{\partial Z^2}, \tag{4}$$

under the following initial and boundary conditions:

$$C_0 = C_i \text{ at } t = 0, \tag{5a}$$

$$D \frac{\partial C_0}{\partial Z} = -R C_0 \text{ at } Z = H(t), \tag{5b}$$

$$\frac{\partial C_0}{\partial Z} = 0 \text{ at } Z = d, \tag{5c}$$

where H(t) is the air-solution interface position and d is the initial solution thickness. So, at a time t, the solution thickness is $d - H(t)$. The evaporation rate, $R(=dH/dt)$, is assumed to be constant [7]. The boundary condition (5b) explains the accumulation of salts at the air-solution interface. Under the assumption of constant evaporation rate, the air-solution interface position can be predicted as

$$H(t) = Rt. \tag{6}$$

The detailed procedure to obtain the above boundary condition (5b) is discussed in Appendix A.

Employing d, d^2/D and C_i as length, time and concentration scaling factors, the above diffusion equations are nondimensionalized as

$$\frac{\partial c_0}{\partial \tau} = \frac{\partial^2 c_0}{\partial z^2}, \tag{7}$$

with the following conditions:

$$c_0 = 1 \text{ at } \tau = 0, \tag{8a}$$

$$\frac{\partial c_0}{\partial z} = -\alpha c_0 \text{ at } z = \alpha \tau, \tag{8b}$$

$$\frac{\partial c_0}{\partial z} = 0 \text{ at } z = 1, \tag{8c}$$

where $\alpha(=Rd/D)$ is the dimensionless evaporation rate. In the deep-pool case of $\tau \ll 1$, where the lower boundary condition, Eq. (8c), plays little role on the concentration field, the last boundary condition can be rephrased as

$$c_0 \to 1 \text{ at } z \to \infty. \tag{9}$$

Using the moving reference frame $\xi = z - \alpha \tau$, and therefore $\partial c_0(\tau, z)/\partial \tau = \partial c_0/\partial \tau + \partial c_0/\partial \xi(\partial \xi/\partial \tau)$, Okuzono et al. [10] reformulate the above base concentration field as

$$\frac{\partial c_0}{\partial \tau} = \frac{\partial^2 c_0}{\partial \xi^2} - \frac{\partial c_0}{\partial \xi}\frac{\partial \xi}{\partial \tau} = \frac{\partial^2 c_0}{\partial \xi^2} + \alpha \frac{\partial c_0}{\partial \xi}, \tag{10}$$

with the following conditions:

$$c_0 = 1 \text{ at } \tau = 0, \tag{11a}$$

$$\frac{\partial c_0}{\partial \xi} = -\alpha c_0 \text{ at } \xi = 0, \tag{11b}$$

$$c_0 \to 1 \text{ as } \xi \to \infty. \tag{11c}$$

Using the Laplace transform method, the following concentration profiles can be obtained (see Appendix B):

$$c_0 = 1 + \alpha \exp\left(-\frac{\alpha \xi}{2}\right) \int_0^\tau \left\{ \frac{1}{\sqrt{\pi \tau'}} \exp\left(-\frac{\xi^2}{4\tau'} - \frac{\alpha^2 \tau'}{4}\right) \right.$$
$$\left. + \frac{\alpha}{2} \exp\left(-\frac{\alpha}{2}\xi\right) \text{erfc}\left(\frac{\xi}{2\sqrt{\tau'}} - \frac{\alpha\sqrt{\tau'}}{2}\right) \right\} d\tau', \tag{12a}$$

$$\frac{dc_0}{d\xi} = -\alpha^2 \exp\left(-\frac{\alpha}{2}\xi\right) \int_0^\tau \left\{ \frac{1}{\sqrt{\pi \tau'}} \exp\left(-\frac{\xi^2}{4\tau'} - \frac{\alpha^2 \tau'}{4}\right) \right.$$
$$\left. + \frac{\alpha}{2} \exp\left(-\frac{\alpha}{2}\xi\right) \text{erfc}\left(\frac{\xi}{2\sqrt{\tau'}} - \frac{\alpha\sqrt{\tau'}}{2}\right) \right\} d\tau', \tag{12b}$$

$$- \frac{\alpha}{2} \left\{ \exp(-\alpha\xi) \text{erfc}\left(\frac{\xi}{2\sqrt{\tau}} - \frac{\alpha\sqrt{\tau}}{2}\right) + \text{erfc}\left(\frac{\xi}{2\sqrt{\tau}} + \frac{\alpha\sqrt{\tau}}{2}\right) \right\}$$

From the above solutions, we can get the concentration and its vertical gradient at the air-solution interface as

$$c_0(\tau, \xi = 0) = 1 + \alpha \int_0^\tau \left\{ \frac{1}{\sqrt{\pi \tau'}} \exp\left(-\frac{\alpha^2 \tau'}{4}\right) + \frac{\alpha}{2} \text{erfc}\left(-\frac{\alpha\sqrt{\tau'}}{2}\right) \right\} d\tau', \tag{13a}$$

$$\left. \frac{\partial c_0}{\partial \xi} \right|_{\xi=0} = -\alpha \left\{ 1 - \alpha \int_0^\tau \left\{ \frac{1}{\sqrt{\pi \tau'}} \exp\left(-\frac{\alpha^2 \tau'}{4}\right) \right. \right. \tag{13b}$$

$$+ \frac{\alpha}{2} \text{erfc}\left(-\frac{\alpha\sqrt{\tau'}}{2}\right) d\tau'\Bigg\} = -\alpha c_0(\tau, \xi=0).$$

Recently, by integrating the base concentration (12), Mossige et al. [6] suggested the following closed form solution:

$$c_0(\xi, \tau) = 1 + \left(\frac{1}{2}\alpha^2\tau - \frac{\alpha}{2}\xi + \frac{1}{2}\right)\text{erfc}(\beta)\exp(-\alpha\xi)$$
$$- \frac{1}{2}\text{erfc}(\gamma) + \alpha\sqrt{\tau}\sqrt{\frac{1}{\pi}}\exp(-\beta^2)\exp(-\alpha\xi), \quad (14a)$$

$$\beta = \frac{\xi}{2\sqrt{\tau}} - \frac{1}{2}\alpha\sqrt{\tau} \text{ and } \gamma = \frac{\xi}{2\sqrt{\tau}} + \frac{1}{2}\alpha\sqrt{\tau}. \quad (14b\&c)$$

The concentration at the interface, $c_{0,h}$, is expressed as

$$c_{0,h}(\tau) = 1 + \left(\frac{1}{2}\alpha^2\tau + \frac{1}{2}\right)\text{erfc}\left(-\frac{1}{2}\alpha\sqrt{\tau}\right)$$
$$- \frac{1}{2}\text{erfc}\left(\frac{1}{2}\alpha\sqrt{\tau}\right) + \alpha\sqrt{\tau}\sqrt{\frac{1}{\pi}}\exp\left(-\frac{\alpha^2\tau}{4}\right). \quad (15)$$

For the limiting case of $\alpha^2\tau \to 0$, the effect of evaporation rate on the concentration field is confined within the narrow region near the solution-air interface, we get the following approximation:

$$c_{0,h} \approx 1 + \sqrt{\frac{4}{D\pi}}R\sqrt{t}, \quad (16a)$$

since

$$c_{0,h}(\alpha^2\tau \to 0) = 1 + \text{erfc}\left(\frac{1}{2}\alpha\sqrt{\tau}\right) + \frac{1}{\sqrt{\pi}}\alpha\sqrt{\tau} \approx 1 + \frac{2}{\sqrt{\pi}}\alpha\sqrt{\tau}, \quad (16b)$$

by using the relations of $\text{erf}(\chi) = \frac{2}{\sqrt{\pi}}\sum_{n=0}^{\infty}\frac{(-1)^n\chi^{2n+1}}{(2n+1)n!}$. Okuzono et al. [10] derived the same result from Eq. (12).

Another solution was given by Dunstan et al. [5]; by transforming the governing equations in the (τ, z)-domain into the (τ', z')-domain, they reformulated Eqs. (7)-(8) as
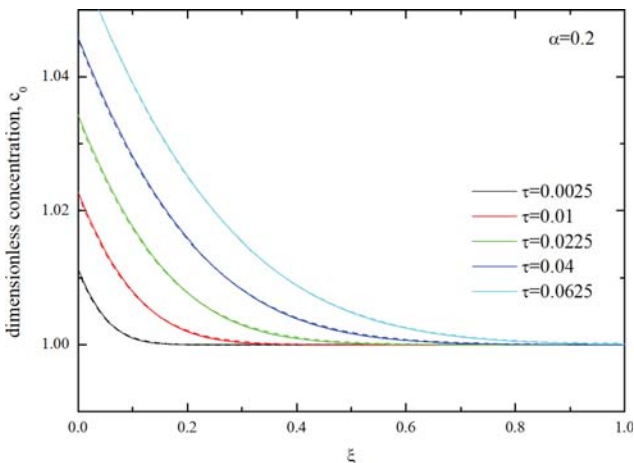

Fig. 2. Base concentration profiles of the salt. The concentration at the air-solution interface, $\xi=0$, increases as the solvent leaves the solution due to the evaporation. Analytic solution (solid lines) and numerical ones (dashed lines) are in good agreement.

$$\frac{\partial c_0}{\partial\tau'} = \frac{1}{H^2}\frac{\partial^2 c_0}{\partial z'^2} - \alpha\frac{z'}{H}\frac{\partial c_0}{\partial z'}, \quad (17)$$

under the following conditions:

$$c_0 = 1 \text{ at } \tau' = 0, \quad (18a)$$

$$\frac{\partial c_0}{\partial z'} = \alpha H c_0 \text{ at } z' = 1, \quad (18b)$$

$$\frac{\partial c_0}{\partial z'} = 0 \text{ at } z' = 0, \quad (18c)$$

where $\tau' = \tau$, $z' = (1-z)/H$, $H = 1 - \alpha\tau$ and $\partial/\partial\tau = \partial/\partial\tau' + \alpha\partial/\partial z'(z'/H)$. Dunstan et al. [5] solved the above equations numerically by using Matlab function "pdepe." The above analytical and numerical solutions are in good agreement, as shown in Fig. 2.

LINEAR STABILITY ANALYSIS

Under linear stability theory, an infinitesimal disturbance caused by incipient convective motion at the dimensionless critical time τ_c can be formulated, in dimensionless form, in terms of the concentration component c_1 and the vertical velocity component w_1 by linearizing Eqs. (1)-(3):

$$\left(\frac{1}{Sc}\frac{\partial}{\partial\tau} - \nabla^2\right)\nabla^2 w_1 = -Ra\nabla_1^2 c_1 \quad (19)$$

$$\frac{\partial c_1}{\partial\tau} + w_1\frac{\partial c_0}{\partial z} = \nabla^2 c_1, \quad (20)$$

where $\nabla^2 = \nabla_1^2 + \frac{\partial^2}{\partial z^2}$, $\nabla_1^2 = \frac{\partial^2}{\partial x^2} + \frac{\partial^2}{\partial y^2}$, $Sc = \frac{\nu}{D}$ and $Ra = \frac{g\beta C_i d^3}{D\nu}$.

Note that the Rayleigh number Ra has the meaning of dimensionless initial concentration. In this study, the velocity component has the scale of D/d. The proper boundary conditions are

$$w_1 = \frac{\partial^2 w_1}{\partial z^2} = 0 \text{ and } \frac{\partial c_1}{\partial z} = -\alpha c_1 \text{ at } z = \alpha\tau, \quad (21a\&b)$$

$$w_1 = \frac{\partial w_1}{\partial z} = c_1 = 0 \text{ at } z = 1, \quad (21b)$$

As for the case of large Ra, the incipient convective motion is confined within a narrow region; the convective length scale, $l \sim (D\nu/g\beta C_i)^{1/3}$, is more appropriate length scale than the solution depth, d. For the case of $Sc \gg 1$, using this convective length scale and the the above stability equations are given as

$$\nabla^4 w_1 = \nabla_1^2 c_1, \quad (22)$$

$$\frac{\partial c_1}{\partial\tau^*} + w_1\frac{\partial c_0}{\partial z^*} = \nabla^2 c_1, \quad (23)$$

where $\tau^*(=Ra^{2/3}\tau) = tD^{1/3}(g\beta C_i/\nu)^{2/3}$ and $z^*(=Ra^{1/3}z) = Z(g\beta C_i/D\nu)^{1/3}$.

Now, convective motion is assumed to exhibit horizontal periodicity and the normal mode analysis is employed. Then the perturbed quantities can be expressed as

$$[w_1(\tau^*, x^*, y^*, z^*), c_1(\tau^*, x^*, y^*, z^*)] \quad (24)$$
$$= [w_1(\tau^*, z^*), c_1(\tau^*, z^*)]\exp[i(k_x x^* + k_y y^*)],$$

where "i" is the imaginary number and the horizontal wavenum-

ber "k" has the relation of $k = (k_x^2 + k_y^2)^{1/2}$. Under this Fourier mode analysis, the hoizontal Laplacian becomes $\nabla_1^2 = -k^2$. Recently, Dunstan et al. [5] solved the above stability Eqs. (22)-(24) under the frozen-time model in the (τ, z)-domain, i.e., $\partial c_1 / \partial \tau = \sigma c_1$, where σ is the growth rate of disturbance in the (τ, z)-domain. However, for a system of large Ra, the incipient convective motion is confined within the narrow penetration region, $\delta \propto \sqrt{Dt}$ [6]. In this case, in the (τ, ζ)-domain, the stability Eqs. (21)-(23) can be reformlated as

$$\left(\frac{\partial^2}{\partial \zeta^2} - k^{*2}\right)^2 w_1 = -k^{*2} c_1, \tag{25}$$

$$\tau^* \frac{\partial c_1}{\partial \tau^*} + \tau^{*3/2} w_1 \frac{\partial c_0}{\partial \zeta} = \left(\frac{\partial^2}{\partial \zeta^2} + \frac{\zeta}{2} \frac{\partial}{\partial \zeta} - k^{*2}\right) c_1. \tag{26}$$

The boundary conditions (21) become

$$w_1 = \frac{\partial^2 w_1}{\partial \zeta^2} = 0 \text{ and } \frac{\partial c_1}{\partial \zeta} = -\alpha^* c_1 \text{ at } \zeta = \alpha^*, \tag{27a\&b}$$

$$w_1 \to 0, \frac{\partial w_1}{\partial z} \to 0, \text{ and } c_1 \to 0 \text{ as } \zeta \to \infty, \tag{27c}$$

where $\zeta = z^* / \sqrt{\tau^*}$, $k^* = k\sqrt{\tau^*}$ and $\alpha^* = \frac{\alpha}{Ra^{1/3}} \sqrt{\tau^*}$. From Eq. (14), the concentration gradient can be rewritten as

$$\frac{\partial c_0}{\partial \zeta} = -\alpha^* \left(\alpha^{*2} - \frac{\alpha^*}{2} \zeta + 1\right) \text{erfc}\left(\frac{\zeta}{2} - \alpha^*\right) \exp(\alpha^{*2} - \alpha^* \zeta)$$
$$- \frac{\alpha^{*2}}{\sqrt{\pi}} \exp\left(-\frac{\zeta^2}{4}\right). \tag{28}$$

Under the quasi-steady state approximation (QSSA), where the growth rates of the disturbances are assumed to be larger than that of the base concentration, the stability Eqs. (26)-(28) are solved by employing the outward shooting scheme [11,12]. For a given α^*, with changing the modified wavenumber k^* and then the neutral stability curves are obtained by setting $\partial c_1 / \partial \tau^* = 0$. For the case of $\alpha^* = 0.01$, the neutral stability curve is given in Fig. 3. According to the present theory, the critical conditions are determined by the
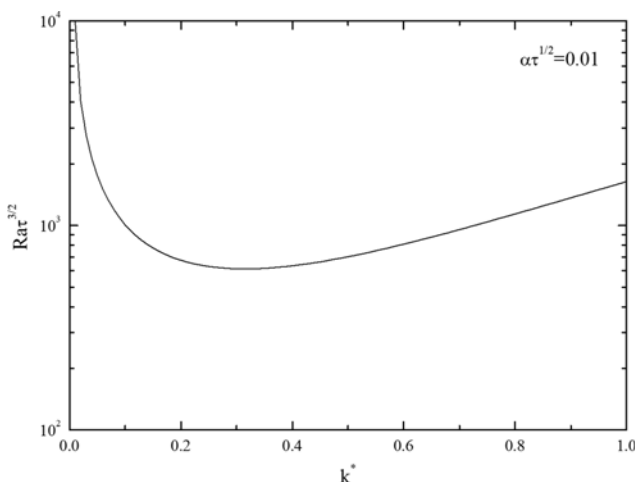

Fig. 3. Neutral stability curve for the case of $\alpha^* = 0.01$. The critical conditions are determined by the minimum point of this curve.

minimum value of τ^* and the corresponding k^*.

NUMERICAL SIMULATION

The above linear analyses are valid only near the critical time. The convective motion driven by solvent evaporation should be studied by solving Eqs. (1)-(3), numerically. Employing d, d^2/D and C_i as length, time and concentration scaling factors, the above diffusion equations are nondimensionalized as

$$\nabla \cdot \mathbf{u} = 0, \tag{29}$$

$$\frac{1}{Sc}\left(\frac{\partial}{\partial \tau} + \mathbf{u} \cdot \nabla\right) \mathbf{u} = -\nabla p + \nabla \cdot \{\nabla \mathbf{u} + (\nabla \mathbf{u})^T\} + Rac\mathbf{k}, \tag{30}$$

$$\left(\frac{\partial}{\partial \tau} + \mathbf{u} \cdot \nabla\right) c = \nabla^2 c, \tag{31}$$

$$\mathbf{u} = \mathbf{0}, \ p = 0 \text{ and } c = 1 \text{ at } \tau = 0, \tag{32a}$$

$$\mathbf{n} \cdot \{\nabla \mathbf{u} + (\nabla \mathbf{u})^T\} = 0 \text{ and } \frac{dc}{dz} = -\alpha c \text{ at } z = 1 - \alpha \tau, \tag{32b}$$

$$\mathbf{u} = \mathbf{0} \text{ and } \frac{\partial c}{\partial z} = 0 \text{ at } z = 0, \tag{32c}$$

$$\mathbf{u} = \mathbf{0} \text{ and } \frac{\partial c}{\partial x} = 0 \text{ at } x = \pm L/2, \tag{32c}$$

The above equations were solved by using the finite element method (FEM) package COMSOL MULTIPHYSICS® [13]. "Laminar Flow" module of the COMSOL was used to solve the continuity Eq. (29) and the Navier-Stokes Eq. (30) with the "Volume Force" option for the buoyancy force. The mass transport Eq. (31) was implemented by using "Transport of Dilute Species" module, where the flow fields were adopted from the Navier-Stokes equation. As water evaporates, the concentration of salt at the air-solution interface increases due to the mass conservation of involatile salt. To implement the condition at the air-solution interface, the interface was allowed to move downward with the evaporation rate, α. Then the inward salt flux, αc_h— where c_h is the concentration of the salt at the moving interface— was added. Slip-wall boundary condition was imposed on the air-solution interface. And the boundary conditions of the lateral and bottom sides were incorporated by the no-slip and no-flux conditions. Geometry and boundary conditions are summarized in Fig. 4.

The COMSOL Multiphysics has a wide variety of options in choosing the time-dependent solver. In the present study, 1st or 2nd
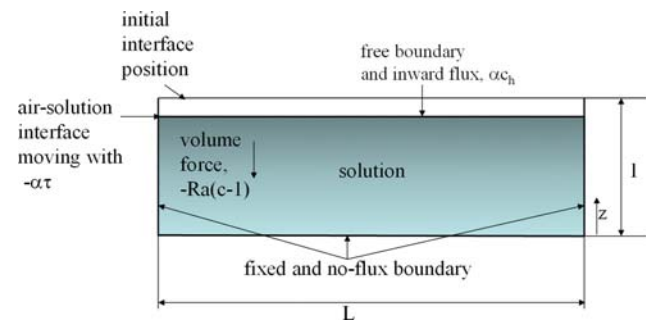

Fig. 4. Schematic diagram of system geometry and boundary conditions used in the present numerical simulations.

order, variable step size, backward differentiation formula (BDF) was used. The order of BDF solver is determined by the degree of the interpolating polynomial. At each time step, the system of non-linear algebraic equation is linearized employing Newton method, and the resulting linearized system is solved by PARDISO direct solver, which is fast, robust, and multi-core capable. The scaled absolute tolerance factors of 0.05 and 1 and were set for the concentration and the pressure, respectively. The relative tolerance was 1×10^{-4}. No critical differences were found by changing these tolerances.

Table 1. Numerical values of the parameters used in the present simulations

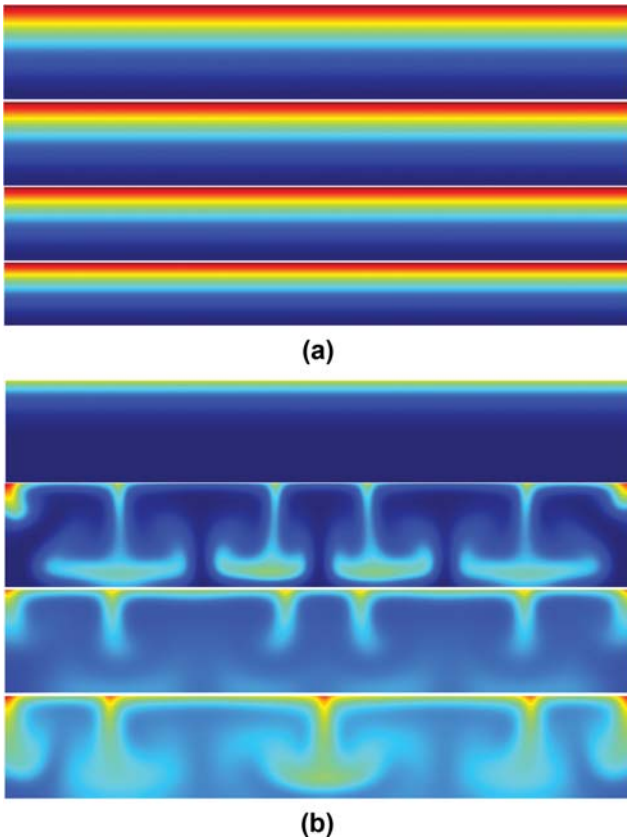| Parameter	Symbol	Value
Kinematic viscosity	ν	10^{-6} m^2/s
Salt diffusion constant	D	10^{-9} m^2/s
Salt densification constant	β	0.007 [%(w/w)]$^{-1}$
Initial height of solution	d	10^{-2} m
Evaporation rate	R	2×10^{-8} m/s
Dimensionless evaporation rate	$\alpha(=Rd/D)$	0.2
Schmidt number	$Sc(=\nu/D)$	10^3

(a)

(b)

Fig. 5. Temporal evolution of the concentration fields. (a) Concentration distributions at (top to bottom) $\tau=0.5$, $\tau=1$, $\tau=1.5$ and $\tau=2$ for the system of Ra=10^3, and (b) concentrations distribution at (top to bottom) $\tau=0.025$, $\tau=0.05$, $\tau=0.075$ and $\tau=0.1$ for the system of Ra=10^6. Red and blue colors represent high and low concentrations, respectively.

In the present study, using Dunstan et al's [5] experimental condition, the Schmidt Sc=1,000 and the aspect ratio L=6 were set. The physical parameters used in the present numerical simulations are summarized in Table 1. We traced the temporal evolution of concentration field by using the following interfacial length:

$$I = \int_{\Omega} |\nabla c| d\Omega = \int_{-L/2}^{L/2} \int_{0}^{H} \sqrt{\left(\frac{\partial c}{\partial x}\right)^2 + \left(\frac{\partial c}{\partial z}\right)^2} \, dz dx. \tag{33}$$

In addition, during the simulation, we checked whether the quantity of the involatile salt is conserved or not by tracing the following mass conservation:

$$\frac{1}{L \times d} \int_{-L/2}^{L/2} \int_{0}^{H} c(\tau, x, z) z dx = \frac{1}{L \times d} \int_{-L/2}^{L/2} \int_{0}^{d} c(\tau=0, x, z) z dx = 1. \tag{34}$$

For Dunstan et al's [5] saline water system where the dimensionless evaporation rate is $\alpha=0.2$. Fig. 5 summarizes the temporal evolution of salt concentration fields. As expected, as time goes on, the depth of solution continuously decreases, whereas the concentration increases. Furthermore, buoyancy-driven instability motion is not observed in the case of low Ra system, i.e., low salt concentration case. However, in the high Ra system, the apparent instability motions are set on at a certain time. As shown in the results for the high Ra system, the number of plumes is not constant, with plumes colliding and merging into new ones. This behavior was also experimentally observed by Dunstan [14].

RESULTS AND DISCUSSION

Fig. 6 summarizes the onset time of buoyancy-driven instability determined from the present linear stability analysis. As expected, the higher the evaporation rate, the earlier the onset of instability. For the limiting case of $\alpha\sqrt{\tau} \to 0$, from Eqs. (17b) and (28b), the base concentration gradient and the boundary conditions for the concentration disturbance at the interface can be approximated as

$$\frac{\partial c_0}{\partial \zeta} = -\alpha\sqrt{\tau} \text{erfc}\left(\frac{\zeta}{2}\right), \tag{35}$$
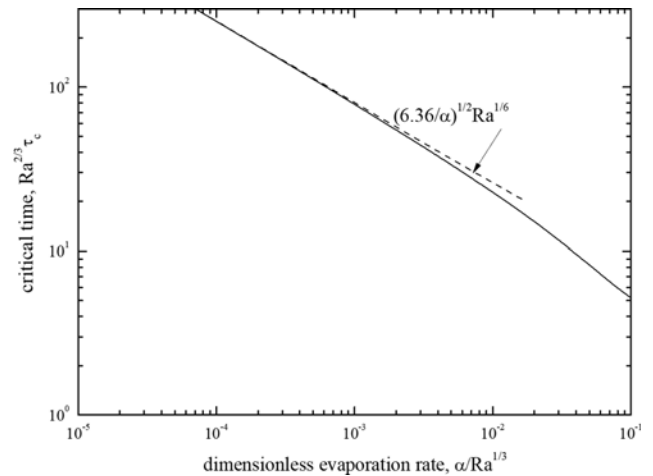

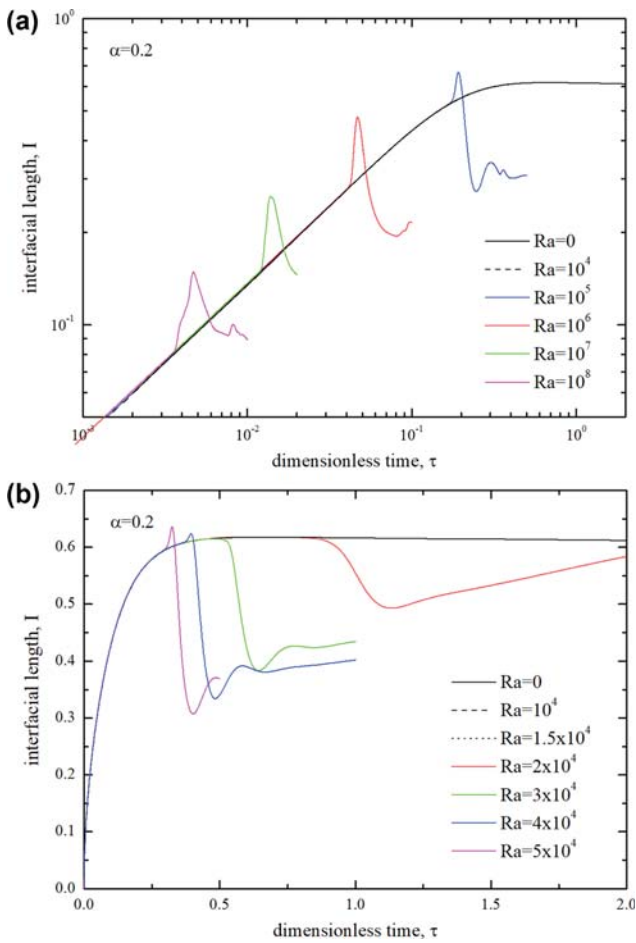**Fig. 6. Effect of the evaporation rate on the critical time from the linear stability analysis.**

Fig. 7. Temporal evolution of the interfacial length for various Ra cases. (a) High Ra cases, and (b) low Ra cases.

$$\frac{\partial c_1}{\partial \zeta} = 0 \quad \text{at} \quad \zeta = 0. \tag{36}$$

For this limiting case, the critical condition obtained by solving the stability Eqs. (26)-(27) with the above approximation is

$$Ra\alpha\tau_c^2 = 6.36 \quad \text{for} \quad \alpha\sqrt{\tau_c} \to 0. \tag{37}$$

For the case of $\alpha/Ra^{1/3} < 10^{-2}$, the above approximation results explain the onset of instability quite well. Fig. 6 suggests that for a given evaporation rate, a longer time was required for the infinitesimal disturbance to start to grow when the salt concentration is lower.

For the comparison between the linear stability analysis and the numerical simulations, Fig. 7 summarizes the temporal evolution of the interfacial length. As shown, for the case of $Ra > 1.5 \times 10^4$, which corresponds to 2.17×10^{-4} wt% salt, the temporal evolution of the interfacial length defined in Eq. (33) deviates from the diffusion dominant system, i.e., low Ra case. In Fig. 8, τ_{max} at which the interfacial length shows its maximum is compared with the critical time determined from the linear analysis. As shown, τ_c from the present linear stability analysis is far below τ_{max} from the present numerical simulation. This discrepancy between the linear analysis and the nonlinear numerical simulation has been found in similar problems [15,16]. It seems that a growing period between τ_c
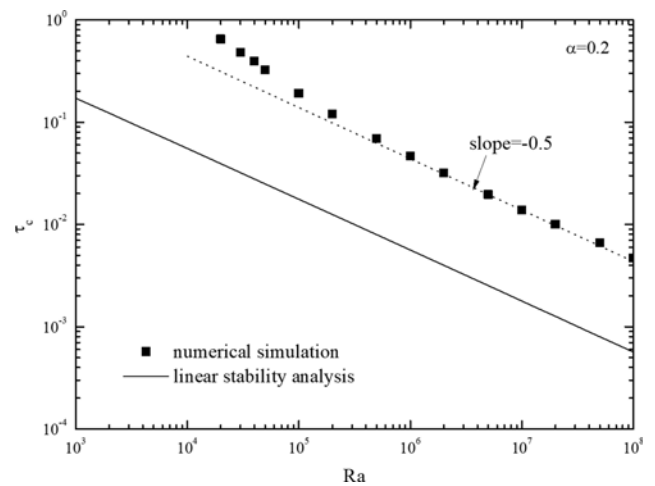

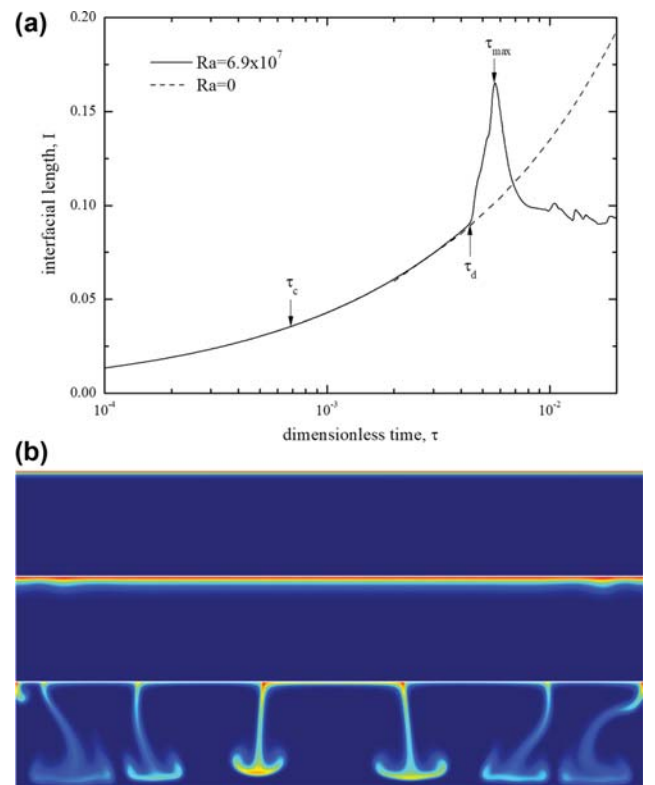**Fig. 8. Comparison of critical times obtained from the linear stability analysis and the numerical simulation.**

Fig. 9. Numerical simulation results for the system of 1% (w/w) salt concentration, which corresponds to Ra=6.9×10^7. (a) Temporal evolution of the interfacial length, and (b) concentration distributions at (top to bottom) $\tau = \tau_c$, $\tau = \tau_d$ and $\tau = \tau_{max}$. Red and blue colors represent high and low concentrations, respectively.

and τ_{max} is required for the infinitesimal disturbance onset at τ_c to be amplified enough. For the case of $Ra > 5 \times 10^5$, the following scaling relation can be used:

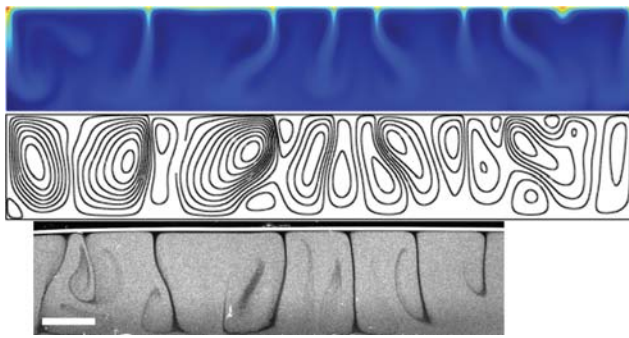$$\tau_{max} \sim (Ra\alpha)^{-1/2} \quad \text{for} \quad Ra > 5 \times 10^5, \tag{38}$$

Fig. 10. Comparison of the present numerical simulation results and the experimental flow visualization for the case Ra=6.9× 10⁷ (1%(w/w)) and τ=0.2 (30 min). The first and second figures are the concentration field and streamlines obtained from the present numerical simulation, and the third image (with permission) is Dunstan's [14] experimental result taken 30 minutes after the experiment. Red and blue colors represent high and low concentrations, respectively. In Dunstan's [14] experiment, a suspension of 3 μm diameter beads with 1%(w/w) salt concentration was used. In the third figure, scale bar is 0.5 cm and dark field image of the plumes.

which can be deduced from the linear stability analysis results, Eq. (37). The relations of Eqs. (37) and (38) reveal that the evaporation-driven instabilities are governed not only by the evaporation rate but also the initial solute concentration.

For the system of 1 wt% salt, which corresponds to Ra=6.9× 10⁷, the temporal evolution of the interfacial length and the normalized concentration fields at τ_c, τ_d and τ_{max} is given in Fig. 9. Under the linear stability theory, we determined τ_c at which the infinitesimal disturbance starts to grow, whereas τ_d corresponds to the time from which the interfacial length deviates from that for the diffusion dominant system. Because, as shown in Fig. 9(a), from the present numerical simulation, the identification of τ_{max} at which the interfacial length has its maximum value is easier than that of τ_d; τ_{max} is also chosen to explain the numerical simulation results. Fig. 9(a) implies that there is a growth period, ($\tau_d-\tau_c$) during which the disturbances onset at τ_c grow enough to be detected experimentally. As shown in Fig. 9(b), the concentration field is kept to being diffusion-dominant state until the deviation time τ_d, and the incipient motion is initiated near the lateral boundary.

From the concentration distribution at $\tau=\tau_{max}$, it is clear that the concentration of involatile salt near the lower surface is non-uniform and, therefore, coffee-stain like structures are inevitable. Dunstan [14] visualized the flow field of 1 wt% salt system by adding 3 μm diameter beads. In Fig. 10, Dunstan's [14] visualization result is compared with the present numerical simulation. Dunstan's [14] plum structure is quite similar to the concentration field obtained from the present numerical simulation. Figs. 9 and 10 show that the spatial structure of plum is not static, i.e., as time goes on, plumes are colliding and merging into new ones and some others are newly generated. This dynamic behavior can be found in Dunstan's [14] and Mossige et al's [6] experiment.

CONCLUSIONS

The onset of evaporation-driven gravitational instability in saline water was analyzed theoretically and numerically. As the evaporation proceeded, the height of solution continuously decreased with time and salt was concentrated near the solution-air interface. For a high salt concentration system, the gravitational instability is onset after a certain diffusion dominant period. However, the gravitational instability has never been observed for a low salt concentration system. The critical time determined from the linear stability analysis explains the numerical simulation results reasonably. From the present numerical simulation, it is clearly shown that there exists a critical salt concentration under which instability motion cannot be expected. In addition, the previous flow visualization results for the evaporation of saline water and the present numerical simulations are in good agreement. The present study can be extended to the study on the effect of solvent evaporation rate on the morphology of the polymeric film formed from polymer solution where the effect of the concentration-dependent viscosity should be considered.

ACKNOWLEDGEMENT

REFERENCES

1. T. D. Foster, *Phys. Fluids*, **8**, 1770 (1965).
2. A. Vidal and A. Acrivos, *Ind. Eng. Chem. Fund.*, **7**, 53 (1968).
3. S. Dehaeck, C. Wylock and P. Colinet, *Phys. Fluids*, **21**, 091108 (2009).
4. K. H. Kang, H. C. Lim, H. W. Lee and S. J. Lee, *Phys. Fluids*, **25**, 042001 (2013).
5. J. Dunstan, K. J. Lee, Y. Hwang, S. F. Park and R. E. Goldstein, *Phys. Rev. Fluids*, **3**, 123102 (2018).
6. E. M. Mossige, V. Chandra Suja, M. Islamov, S. F. Wheeeler and G. G. Fuller, *Phil. Trans. R. Soc. A*, **378**, 20190533 (2019).
7. G. Toussaint, H. Bodiguel, F. Doumenc, B. Guerrier and C. Allain, *Int. J. Heat Mass Transfer*, **51**, 4228 (2008).
8. Q. Fang, F. Ye and X. Yang, *Langmuir*, **34**, 5551 (2019).
9. B. Sobac, P. Colineta and L. Pauchard, *Soft Matter*, **15**, 2381 (2019).
10. T. Okuzono, K. Ozawa and M. Doi, *Phys. Rev. Lett.*, **97**, 136103 (2006).
11. M. C. Kim, *Korean Chem. Eng. Res.*, **57**, 142 (2019).
12. M. C. Kim, *Korean Chem. Eng. Res.*, **57**, 723 (2019).
13. COMSOL Multiphysics, ver. 5.4 COMSOL AB, Stockholm, Sweden (2019).
14. J. Dunstan, *Convective flows generated by evaporation*, PhD theis, University of Cambridge, UK (2018).
15. W. S. Ryoo and M. C. Kim, *Korean J. Chem. Eng.*, **35**, 1247 (2018).
16. W. S. Ryoo and M. C. Kim, *Korean J. Chem. Eng.*, **35**, 1423 (2018).

APPENDIX A

The boundary conditions for the concentration of an involatile salt at the free surface are discussed here. From the following material balances for the solvent and involatile salt:

$$\frac{d}{dt}\left\{\int_{H(t)}^{d}(1-C)dZ\right\}=-R \ \text{ and } \ \frac{d}{dt}\left\{\int_{H(t)}^{d}CdZ\right\}=0, \tag{A1}$$

and the Leibniz integral rule, we get the following relations:

$$-\frac{\partial H}{\partial t}+C_H\frac{\partial H}{\partial t}-\int_{H(t)}^{d}\frac{\partial C}{\partial t}dZ=-R \ \text{ and } \ -\frac{\partial H}{\partial t}C_H+\int_{H(t)}^{d}\frac{\partial C}{\partial t}dZ=0. \tag{A2}$$

By integrating the governing Eq. (4) and then applying the boundary condition (5c), the last terms of the left-hand side of the above equations become

$$\int_{H(t)}^{d}\frac{\partial C}{\partial t}dZ=\int_{H(t)}^{d}D\frac{\partial^2 C}{\partial Z^2}dZ=D\frac{\partial C}{\partial Z}\bigg|_{d}-D\frac{\partial C}{\partial Z}\bigg|_{H(t)}=-D\frac{\partial C}{\partial Z}\bigg|_{H(t)}. \tag{A3}$$

By combining the above relations, we can get the following boundary conditions at the air-solution interface:

$$\frac{\partial H}{\partial t}=R \ \text{ and } \ -RC=D\frac{\partial C}{\partial Z} \ \text{ at } \ Z=H(t), \tag{A4}$$

which is equivalent to the boundary condition (5b)

APPENDIX B

From Eqs. (10) and (11a), we get the following transformed equation:

$$s\mathcal{L}(c_0)-1=\frac{d^2}{d\xi^2}\mathcal{L}(c_0)+\alpha\frac{d}{d\xi}\mathcal{L}\{c_0\}, \tag{B1}$$

where the Laplace transform of c_0 is defined as

$$\mathcal{L}\{c_0(\tau',\xi)\}=\bar{c}_0(s,\xi)\equiv\int_0^\infty \exp(-s\tau')c_0(\tau',\xi)dt'. \tag{B2}$$

The general solution of Eq. (A1) is

$$\bar{c}_0(s,\xi)=\frac{1}{s}+d_1\exp(\lambda_1\xi)+d_2\exp(\lambda_2\xi), \tag{B3}$$

where

$$\lambda_1=-\frac{\alpha}{2}-\sqrt{p} \ \text{ and } \ \lambda_2=-\frac{\alpha}{2}+\sqrt{p}, \tag{B4}$$

where $p=s+\alpha^2/4$. To satisfy the boundary condition (11c), which corresponds to $\bar{c}_0\rightarrow 1/s$ as $\xi\rightarrow\infty$, the undetermined constant d_2 should be zero, i.e.,

$$\bar{c}_0(s,\xi)=\frac{1}{s}+d_1\exp(\lambda_1\xi). \tag{B5}$$

By using the boundary condition (11b), which is equivalent to $\bar{c}_0(s,0)=-\alpha\dfrac{d\bar{c}_0}{d\xi}\bigg|_{\xi=0}$, the remaining constant d_1 should be determined, and therefore, we get the following solutions:

$$\bar{c}_0(s,\xi)=\frac{1}{s}+\alpha\exp\left(-\frac{\alpha\xi}{2}\right)\frac{1}{s}\frac{1}{\sqrt{p}-\alpha/2}\exp(-\sqrt{p}\xi), \tag{B6}$$

$$\frac{d\bar{c}_0}{d\xi}=-\alpha\left(\bar{c}_0-\frac{1}{s}\right)-\alpha\exp\left(-\frac{\alpha\xi}{2}\right)\frac{1}{s}\exp(-\sqrt{p}\xi), \tag{B7}$$

By using the following inverse Laplace transform:

$$\mathcal{L}^{-1}\left\{\frac{1}{\sqrt{p}-\alpha/2}\exp(-\sqrt{p}\xi)\right\}=\frac{1}{\sqrt{\pi\tau}}\exp\left(-\frac{\xi^2}{4\tau}-\frac{\alpha^2\tau}{4}\right)$$
$$+\frac{\alpha}{2}\exp\left(-\frac{\alpha}{2}\xi\right)\text{erfc}\left(\frac{\xi}{2\sqrt{\tau}}-\frac{\alpha\sqrt{\tau}}{2}\right), \tag{B8}$$

$$L^{-1}\left\{\frac{1}{s}\exp(-\sqrt{p}\xi)\right\}=\frac{1}{2}\left\{\exp\left(-\frac{\alpha}{2}\xi\right)\text{erfc}\left(\frac{\xi}{2\sqrt{\tau}}-\frac{\alpha\sqrt{\tau}}{2}\right)\right.$$
$$\left.+\exp\left(\frac{\alpha}{2}\xi\right)\text{erfc}\left(\frac{\xi}{2\sqrt{\tau}}+\frac{\alpha\sqrt{\tau}}{2}\right)\right\}, \tag{B9}$$

and introducing the convolution integral, we get Eqs. (12a) and (12b).